

Generation of a wave packet tailored to efficient free space excitation of a single atom

Andrea Golla,^{1,2} Benoît Chalopin,^{2,3} Marianne Bader,^{1,2} Irina Harder,² Klaus Mantel,²
Robert Maiwald,^{1,2} Norbert Lindlein,¹ Markus Sondermann,^{1,2,*} and Gerd Leuchs^{1,2}

¹*Institute of Optics, Information and Photonics,
University of Erlangen-Nuremberg, 91058 Erlangen, Germany*

²*Max Planck Institute for the Science of Light, 91058 Erlangen, Germany*

³*Laboratoire Collisions Agrégats Réactivité - UMR5589,
Université Paul Sabatier - Bât. 3R1b4, 31062 Toulouse Cedex 09, France*
(Dated: July 16, 2012)

We demonstrate the generation of an optical dipole wave suitable for the process of efficiently coupling single quanta of light and matter in free space. We employ a parabolic mirror for the conversion of a transverse beam mode to a focused dipole wave and show the required spatial and temporal shaping of the mode incident onto the mirror. The results include a proof of principle correction of the parabolic mirror's aberrations. For the application of exciting an atom with a single photon pulse we demonstrate the creation of a suitable temporal pulse envelope. We infer coupling strengths of 89% and success probabilities of up to 87% for the application of exciting a single atom for the current experimental parameters.

The final publication is available at www.epj.org.

I. INTRODUCTION

In the last decades light-matter interaction has been studied in a large variety of experiments not only in many body systems such as atomic ensembles, where coherent laser pulses are transferred and stored to a collective excitation [1, 2], but also on the level of single matter particles. Efficient coupling of single atoms to single photons has been demonstrated by locating an atom inside an optical cavity [3–6]. Such efficient coupling is mandatory in many proposals for quantum information protocols which rely on quantum memories and processors, i.e., on the efficient interaction of a quantum state of light with the internal quantum states of matter. Light is a fast and robust way to transmit quantum information, but the transfer over long distances requires quantum repeaters based on such quantum memories [7–9]. The rate of information transfer through the quantum channel depends on the process efficiency of both storage and read-out. Such efficient coupling can be achieved using a cavity based scheme and accepting the corresponding modification of the mode spectrum from continuous to discrete.

An alternative – and quite natural – approach is the coupling in *free space*. In this approach, the *direct* coupling of light to matter has to be maximized instead of the coupling to a cavity. Besides their potential use in various applications, efficient free space coupling schemes offer large design freedom. They enable the investigation of light-matter interaction without modifying the density of states of the electromagnetic field continuum. Alternatively one can study the effect of, e.g., a modified quantum vacuum [10].

Recently, one could witness increased efforts devoted to the topic of efficient free space coupling. When discussing the corresponding advances one can clearly distinguish between two different processes: One is the elastic scattering of a laser beam by an interacting particle for which no substantial excitation of the matter system occurs, i.e., the probability to find the matter system in its excited state is low throughout the interaction process. The efficient elastic scattering manifests itself in the attenuation of a weak coherent laser beam resonant with a transition of the interacting particle, as has been shown for single molecules [11], single quantum dots [12], single atoms [13] or single ions [14]. Another hallmark of efficient elastic scattering is the phase shift of a weak laser beam detuned from resonance, which was demonstrated recently for the free space scenario [15, 16]. Corresponding theoretical contributions can be found in Refs. [17–21].

The other process treated in recent literature is the process of efficient absorption of a photon by a single atom, i.e., the matter system is to be brought to its excited state with high probability. Note that this should not be confused with a π -pulse. While a π -pulse – typically containing many photons – transfers the atom efficiently to the excited state the pulse cannot be fully absorbed by a single atom. Furthermore, the rotation angle of the Bloch vector (e.g. π) is given by time integrating the electric field envelope, while a single photon Fock state has a zero electric field expectation value. Theoretical and conceptual contributions devoted to the absorption of single photons can be found in Refs. [22–27]. A recent experimental demonstration of the absorption of a single photon by a single atom was given by Piro et al [28], whereas an early demonstration of reduced transmission of a bright laser beam by a single ion was performed by Wineland et al [29].

It is common to the two processes of elastic scattering and absorption of a photon that their efficiencies are proportional to the extent to which the incident light mode

* Markus.Sondermann@physik.uni-erlangen.de

resembles an electric dipole wave [19, 20, 22, 23, 25]. More precisely, the spatial properties of the incident light mode should match the ones of the wave that would emerge from the dipole moment of the interacting particle. Here, we show how to experimentally generate such a dipole wave envisioning close to optimum coupling efficiencies. As outlined below, we do this by preparing a plane light wave that, after reflection off a parabolic mirror, is transformed into a dipole wave [23, 24]. An essential property of this setup is that the parabolic mirror covers nearly the complete solid angle surrounding the dipolar absorber.

For the specific aim of perfectly exciting a single two-level atom with a single photon one may take guidance from the spontaneous emission process: The incident photon must resemble the time reversed version of a spontaneously emitted photon [22–24]. This includes the dipole properties discussed above. Furthermore, time reversal arguments demand that the temporal envelope of the incident photon is exponentially increasing with a time constant equal to the lifetime of the atom's excited state [24]. This heuristic approach has been confirmed by detailed calculations [26].

There exist several methods for temporal shaping of single photons in general. One approach is to shape the photon during its creation process, for instance by temporal modulation of the intensity of the control laser in schemes based on electromagnetically induced transparency [30] or by modulation of the pump beams driving the process of four wave mixing [31] or parametric down-conversion (PDC) [32]. Also the shaping of single photons by spectrally filtering one of two PDC photons has been demonstrated [33]. In the case of single photon generation with a single emitter located inside an optical resonator [34–37] the temporal modulation of the pump laser intensity changes the emitted single photon waveform. Furthermore a heralded single photon can also be modulated directly using electro-optic modulation [38, 39].

However, with the mentioned techniques it is challenging to generate a single photon Fock state with an exponentially increasing temporal envelop, especially at wavelengths in the ultraviolet spectral range (which are of interest in this paper, see below). Instead we use coherent laser pulses which are highly attenuated to less than one photon per pulse. This procedure is often used as a substitute for generating single photon Fock states [40]. For the sake of simplicity, we will use the term 'single photon' also for strongly attenuated coherent states, keeping in mind that all excitation probabilities mentioned in this paper are strictly valid only for true single photon wave packets. Nevertheless, if the amplitude of the coherent state is low enough, contributions from Fock states with photon numbers larger than one are negligible. It is then a good approximation to apply the excitation probabilities for true single photon states to that instances of the coherent state wave packets that would be projected onto a single photon state upon measuring the photon

Ion	Transition	Wavelength (λ)	Lifetime (τ)	Label
$^{174}\text{Yb}^+$	$^2\text{S}_{1/2} \rightarrow ^2\text{P}_{1/2}$	369.5 nm	8.1 ns	T1
$^{174}\text{Yb}^{2+}$	$^1\text{S}_0 \rightarrow ^3\text{P}_1$	251.8 nm	230 ns	T2

TABLE I. Overview of the dipole transitions treated exemplarily in this paper. Lifetime data are taken from Refs. [41, 42]. The labels T1 and T2 will be used in the text for the sake of simplicity.

number.

In what follows, we present and characterize experimental techniques to produce the optimal optical mode for perfectly coupling light with an atomic dipole, especially for the case of exciting a single atom with a single photon. The paper is organized as follows: In the next section we motivate a measure for the coupling strength between a single atom (or any other matter system) and light and relate this measure to the absorption efficiency. In Sec. III the experimental generation of a radially polarized Laguerre-Gauss mode is shown. We present the characterization of this beam and calculate the overlap of the experimental data with the optimal dipole wave. Another property of dipole waves is their uniform phase. Therefore, it is essential to compensate for phase aberrations of the device that focuses the incident light towards the matter particle. This topic is treated in Sec. IV. Section V is devoted to the shaping of the temporal properties of a weak coherent state with the aim of maximizing absorption. This aspect as well as the spatial mode shaping is exemplified for two specific linear dipole transitions of singly and doubly ionized Ytterbium, but the corresponding schemes can be adapted to any dipole transition. The properties of our exemplary transitions are listed in table I. Finally, in the last section we estimate the coupling efficiencies and absorption probabilities that would be achieved when interfacing the generated light waves with the corresponding single ions.

II. DEFINITION OF THE FREE SPACE COUPLING STRENGTH

The coupling constant of the interaction of light and matter in the dipole approximation is given by the Rabi frequency $g \sim \vec{\mu} \cdot \vec{E}/\hbar$ in free space as well as in an optical resonator, where $\vec{\mu} = \mu \cdot \vec{e}_\mu$ is the atomic dipole moment and \vec{E} the electric field. Depending on whether the treatment is semi-classical or fully quantized, $\vec{\mu}$ alone or both $\vec{\mu}$ and \vec{E} are operators, respectively. In either case a large coupling constant requires a large portion of the incident electric field to be parallel to the atomic dipole.

In cavity quantum electro-dynamics the coupling strength is proportional to g^2 . Here, we adopt this measure (cf. Ref. [24]) and define the free space coupling strength G as the electric energy density in the focus that corresponds to the field component parallel to the atomic dipole and normalize it to the maximum possible

one for a given input power:

$$G = \frac{|\vec{E} \cdot \vec{e}_\mu|^2}{|E_{\max}|^2} \quad (1)$$

In the focus, the electric field component along a specific dipole moment is proportional to the square root of the solid angle covered by the mediating focusing optics Ω_μ and to the overlap η of the incident field with the dipole field distribution \vec{E}_μ [43]: $\vec{E} \cdot \vec{e}_\mu \sim \sqrt{\Omega_\mu} \cdot \eta$. It should be noted that Ω_μ is the solid angle weighted with the angular dipole radiation pattern $D(\vartheta)$: $\Omega_\mu = \int D(\vartheta) \sin \vartheta d\vartheta d\varphi$. The overlap

$$\eta = \frac{\int \vec{E}^* \cdot \vec{E}_\mu \sin \vartheta d\vartheta d\varphi}{\sqrt{\int |\vec{E}|^2 \sin \vartheta d\vartheta d\varphi \cdot \int |\vec{E}_\mu|^2 \sin \vartheta d\vartheta d\varphi}} \quad (2)$$

is calculated integrating over the solid angle covered by the focusing optics [43]. The maximum values of these quantities are $\Omega_\mu^{\max} = 8\pi/3$ and $\eta^{\max} = 1$. Therefore, the free space coupling strength is written as

$$G = \frac{3}{8\pi} \cdot \Omega_\mu \cdot \eta^2 \quad (3)$$

It reaches unity only if the full solid angle is covered by the focusing optics and the mode matching is perfect. Likewise the maximum coupling strength for half solid angle illumination is $G = 0.5$. These values correspond to the 'scattering ratios' of four and two, respectively, as used by Tey et al [21] and Zumofen et al [20].

G can be interpreted as a geometric quantity that is determined by the focusing setup and the spatial properties of the incident light mode. For a classical field or a coherent state wave packet \sqrt{G} scales the field amplitude at the focus (or its expectation value, respectively). If the incident light field is a Fock state, \sqrt{G} scales the magnitude of the uncertainty of the incident field at the focus.

While $G = 1$ is necessary for reaching the maximum effect in all sorts of free space interaction (phase shifts, scattered power, absorption, etc.) it is not sufficient for reaching unit probability during the absorption of a single photon by a single atom. As mentioned above, the temporal profile of the single photon wave packet plays a decisive role. The optimum effect, i.e., 100% excitation of a two-level atom can only be obtained if the temporal profile matches an increasing exponential with proper time constant [24, 26, 27]. To quantify deviations from this profile we introduce the temporal overlap η_t of the incident field amplitude $E_{\text{inc}}(t)$ with the amplitude $E_{\text{ideal}}(t) = e^{\frac{\Gamma}{2}t} \cdot \theta(-t)$ of the ideal pulse shape:

$$\eta_t = \frac{\int_{-\infty}^{\infty} E_{\text{inc}}(t) \cdot E_{\text{ideal}}(t) dt}{\sqrt{\int_{-\infty}^{\infty} |E_{\text{inc}}(t)|^2 dt / \Gamma}} \quad (4)$$

$\theta(t)$ is the Heaviside function and Γ the spontaneous emission rate of the two-level system to be excited. This

overlap can be considered as a generalization of Eq. (8) of Ref. [26] which treats the case of an exponentially increasing pulse amplitude. It is assumed that the incident signal is shifted in time by an amount that maximizes η_t . Since the respective equation in Ref. [26] determines the probability amplitude to find an atom in the excited state, we take η_t^2 as a multiplicative factor determining the absorption probability

$$P_a = G \cdot \eta_t^2 = \frac{3}{8\pi} \cdot \Omega_\mu \cdot \eta^2 \cdot \eta_t^2 \quad (5)$$

The prospective coupling efficiencies G and absorptions probabilities P_a based on the experimentally achieved overlaps will be given in Sec. VI.

III. GENERATION OF THE OPTIMUM SPATIAL MODE

A dipole wave incident from nearly the full solid angle is generated by reflection of a collimated laser beam from a deep parabolic mirror. The ideal beam shape incident on the parabolic mirror is the time reversed version of a dipole wave that emerges from the focus of the mirror and is reflected at the parabolic surface. After reflection off the parabolic mirror the field vector \vec{E}_μ of light emitted by a linear dipole located at the focal point and with the quantization axis along the mirror axis is described by [23, 43]

$$\vec{E}_\mu \left(\frac{r}{f} \right) = E_0 \cdot \frac{\frac{r}{f}}{\left[\left(\frac{r}{2f} \right)^2 + 1 \right]^2} \cdot \vec{e}_r \quad (6)$$

where f is the focal length of the mirror, \vec{e}_r the unit vector in radial direction, E_0 is an amplitude factor and a factor $\exp(i\vec{k}\vec{r})$ has been omitted. This field distribution has to be generated by an optical element from an incoming plane wave. The amplitude distribution of this ideal mode can in principle be created using diffractive optical elements. However, there are several drawbacks to this method [23]. Instead we generate a radially polarized doughnut beam which can have a large overlap with the ideal mode and can be created without using diffractive optics.

The field vector \vec{E}_{rpd} of a radially polarized doughnut mode can be expressed as

$$\vec{E}_{\text{rpd}} \left(\frac{r}{f} \right) = E_0 \cdot \frac{r}{f} \cdot e^{-\frac{(r/f)^2}{(w/f)^2}} \cdot \vec{e}_r \quad (7)$$

The overlap of the radially polarized doughnut mode with the ideal distribution is optimized by adjusting the beam radius w with the maximum achievable overlap depending on the magnitude of the weighted solid angle Ω_μ (i.e., the depth of the mirror with respect to its focal length or the half opening angle) [43]. Our parabolic mirrors have a

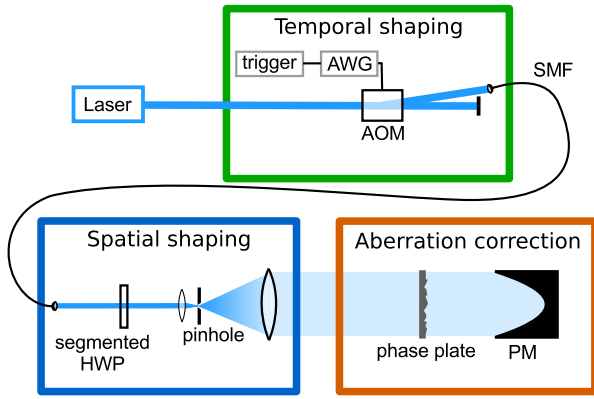


FIG. 1. Experimental setup. The temporal profile is formed using an arbitrary waveform generator (AWG) which determines the temporal envelope of the light power scattered into the first diffraction order of an acousto optical modulator (AOM). The output of the AOM is filtered by a single mode fiber (SMF). Linearly polarized light is sent through a segmented half wave plate (HWP). Subsequently the produced doughnut mode is filtered by a pinhole aperture and expanded to appropriate dimensions. The aberrations of the parabolic mirror (PM) are compensated using a phase plate.

focal length of $f = 2.1$ mm and a front aperture radius of 10 mm. This corresponds to a length of $5.67 \cdot f$ (aperture radius $r_{\text{max}}/f = 4.76$, half opening angle of 134°) and a weighted solid angle for a linear dipole of $\Omega_\mu = 0.94 \cdot \frac{8\pi}{3}$. The maximum possible overlap for this geometric parameters is $\eta = 0.982$ for a beam radius $w = 2.26 \cdot f$ [43]. This limits the experimentally achievable coupling strength G and absorption probability P_a to 0.91. A bore of 0.75 mm radius concentric to the optical axis of the mirror (cf. Sec. IV) induces only negligible changes to Ω_μ and η .

There are different methods for producing a radially polarized doughnut beam. Examples are the use of sub-wavelength dielectric gratings [44, 45], nematic liquid crystals [46] and the coherent addition of the two modes TEM_{01} and TEM_{10} inside laser cavities [47] or interferometers [48, 49]. We use a segmented half-wave plate similar to the one described in Refs. [50, 51] to generate the radially polarized doughnut beam. It consists of $n = 8$ segments of a low order half-wave plate suitable for both wavelengths (370 nm and 252 nm). The experimental setup to generate the doughnut mode is shown in Fig. 1. A continuous wave laser beam at the wavelength of interest first passes the setup for temporal pulse shaping (cf. Sec. V). It is then sent through a polarization maintaining single mode fiber (370 nm beam) or a filtering telescope with a pinhole aperture (252 nm beam), respectively. The resulting linearly polarized Gaussian beam is centered onto the segmented half-wave plate where its polarization is rotated in every segment by an angle of $2\pi/n$, obtaining a full 2π rotation of the electrical field vector over the whole beam cross section. After propagation through the segmented

half-wave plate the beam contains the radially polarized doughnut mode and modes of higher order. The latter ones are filtered out using a pinhole aperture in the focal plane of a Keplerian telescope. With this setup the doughnut mode is generated with a power efficiency of 70%.

The polarization properties of the generated doughnut beam are determined performing spatially resolved measurements of the Stokes parameters based on the method described in Ref. [52]. The profile of a beam sent through a rotatable quarter-wave plate and a non rotatable linear polarizer is measured with a CMOS camera. Due to the technical limitations of the CMOS camera the Stokes measurements are not performed with single photon pulses but with continuous wave laser light.

Once the Stokes parameters are measured the total intensity S_0 and the characteristic angles of the polarization ellipse are calculated for every camera pixel. Since the CMOS camera chip used in the Stokes measurements is much smaller than the front aperture of the parabolic mirror, the measurements have been performed before the final magnification step. Nevertheless, the data are presented in a coordinate system scaled such that the beam radius of the measured doughnut mode matches the optimum beam radius predicted by theory. The results are shown in Figs. 2 and 3 for 370 nm and 252 nm, respectively.

The orientation angle $\psi \in [0, \pi]$ describes the rotation of the main axis of the polarization ellipse with respect to the x-axis. As shown in Figs. 2b) and 3b), at both wavelengths ψ covers the full range of 0 to π in the lower and the upper half plane of the beam cross section. The value of ψ changes continuously with rotation around the beam center. The relative phase of the electric field is the same in both half planes, otherwise a defect line would be observed in S_0 at the $y = 0$ line where ψ jumps from zero to π . Hence, the orientation of the polarization vector is radial on the majority of the beam cross section. Deviations from this behavior occur mainly for radii $\gtrsim 3.5 \cdot f$, i.e., in regions of low intensity. We attribute these deviations to measurement noise originating from the discretization of the camera pixels' intensity values. Furthermore, measurement noise is particularly cumbersome in the vicinity of the x-axis, since there it leads to fluctuations between values of $\psi = 0$ and $\psi = \pi$. When calculating the overlap with an ideal, noise-free state of polarization (performed below) these fluctuations lead to pixels on which the scalar product of the field vectors becomes negative. For pixels with a large value of S_0 this results in a measurement-induced reduction of the overlap integral.

The second angle describing the polarization ellipse is the ellipticity angle $\chi \in [-\pi/4, \pi/4]$ giving the amount of elliptical polarization. Figs. 2c) and 3c) show the ellipticity angles over the cross section of the generated doughnut beams. On the majority of the beam cross section the ellipticity angle is rather low, i.e., the local state of polarization can be regarded as linear with a

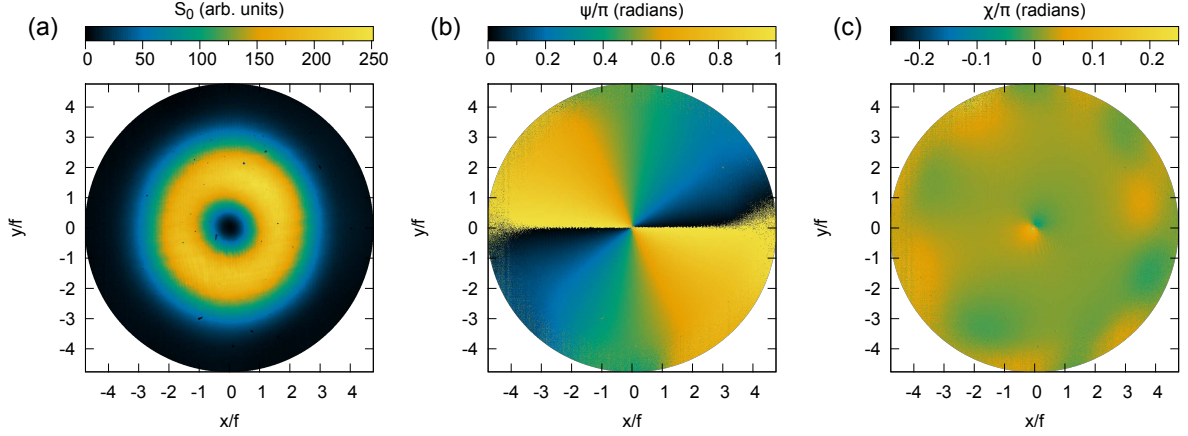


FIG. 2. Characterization of the radially polarized doughnut beam at 370 nm (transition T1): (a) Stokes parameter S_0 (total intensity). (b) Orientation angle ψ . (c) Ellipticity angle χ . The shown data points cover the aperture of the parabolic mirror.

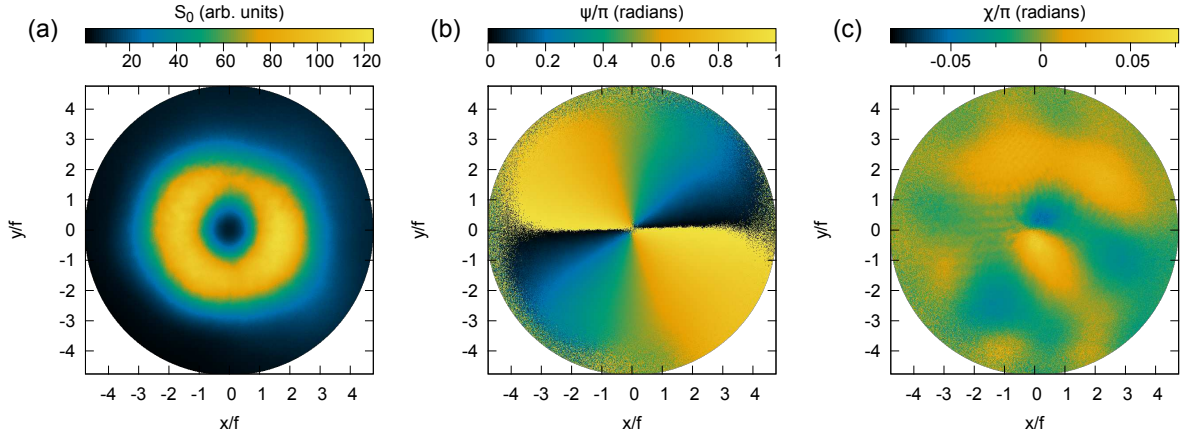


FIG. 3. Characterization of the radially polarized doughnut beam at 252 nm (transition T2): (a) Stokes parameter S_0 (total intensity). (b) Orientation angle ψ . (c) Ellipticity angle χ . The shown data points cover the aperture of the parabolic mirror.

radial orientation.

Next we calculate the overlap of the ideal electric dipole field and the generated radially polarized doughnut mode in the entrance plane of the focusing parabolic mirror, assuming perfect reflection at the mirror surface. This gives the same value as calculating the mode overlap on a sphere close to the focal point, as described in Ref. [43]. The integration is performed over the mirror aperture, i.e., only pixels lying within the boundary $r \leq r_{\max} = 4.76 \cdot f$ are contributing. The spatial field overlap η of the measured radially polarized doughnut beam with the ideal dipole distribution reflected at the mirror is calculated by taking the normalized scalar product of the electric fields

$$\eta = \frac{\int E_{\text{meas}}^* \cdot \vec{e}_{\text{meas}}^* \cdot \vec{E}_{\mu} r dr d\phi}{\sqrt{\int |E_{\text{meas}}|^2 r dr d\phi \int |\vec{E}_{\mu}|^2 r dr d\phi}} \quad , \quad (8)$$

where \vec{e}_{meas} is the normalized measured polarization vector constructed from the angles ψ and χ . E_{meas} is calculated by taking the square root of the measured intensity distribution (the Stokes parameter S_0) and \vec{E}_{μ} is given by Eq. (6). Equation (8) is the equivalent to Eq. (2).

For the mode driving transition T1 we calculate the field overlap of the generated radially polarized doughnut mode with the ideal dipole wave to be 0.963. If we assume perfect orientation angles for the measured beam, i.e., we disregard the discretization effects discussed above, we find $\eta_{370} = 0.979$. The overlap of the generated doughnut mode for transition T2 with the ideal dipole mode is calculated to be 0.939. Assuming ideal orientation angles we arrive at $\eta_{252} = 0.975$.

Our parabolic mirrors are made from aluminum. One might wonder whether the radially varying amplitude of the reflection coefficient, which is due to the radially varying angle of incidence, might influence the obtainable

overlaps (see also Sec. IV). Accounting for the radial variation of the reflectivity in calculating the overlap of the modes given by Eqs. (6) and (7) leads to a slight increase by 0.03% in comparison to the maximum obtainable mode overlap for constant reflectivity.

Therefore, we conclude that the obtainable overlaps are not influenced by the material properties of aluminum in a significant way.

IV. ABERRATION CORRECTION

An essential prerequisite for generating dipole modes is an aberration free phase front: The phase of the focused wave should be uniform on a spherical surface enclosing the focal point. Such an ideal spherical wave can only be generated if the parabolic mirror is free of surface deviations. Since any realistic device has aberrations (see, e.g., Refs. [53–55]), these need to be characterized and corrected for. Ideally the wavefront incident onto the parabolic mirror can be shaped such as to create an aberration free inward moving spherical wave after reflection off the mirror.

One method of measuring the imperfections of a parabolic mirror is to scan its surface using a profilometer [54, 55]. But the huge relative depth of our parabola makes it hardly accessible for profilometer heads. We measure the shape deviations by interferometry with nanometer accuracy [53]. Let us briefly recall the core features of the interferometer setup, details can be found in Ref. [53]. We use an interferometer of the Fizeau type at the standard helium-neon laser wavelength $\lambda_{\text{HeNe}} = 632.8$ nm. A reference wave is produced at a wedged fused silica plate with surface flatness $\leq \lambda/100$. A small steel (or glass) sphere located concentric to the focus of the parabolic mirror is acting as a null element. Any light ray traveling parallel to the optical axis of the parabola is reflected towards the sphere, reflected back onto its path of incidence and interferometrically overlapped with the reference beam. Owing to this double pass geometry, we measure twice the phase aberration introduced by the mirror. Possible aberrations of the sphere are eliminated by averaging over different spheres and different rotational orientations of each sphere relative to the parabolic mirror. The deviations from a perfect parabola obtained after removal of misalignment aberrations are finally represented by Zernike polynomials.

Our parabolic mirrors are made of diamond turned aluminum and are produced at the Fraunhofer Institute for Applied Optics and Precision Engineering at Jena (see Sec. III for the geometric parameters). A central on axis bore of 1.5 mm diameter is used for locating the sphere or any other object such as an ion [56] in the focal point.

The interferometric measurements are performed with a radially polarized doughnut beam centered on the optical axis of the parabolic mirror. In this particular case light is polarized parallel to the plane of incidence at every spot on the surface of the parabolic reflector.

Figure 4a) shows the result of such a measurement for one of our parabolic mirrors. The peak-to-valley (PV) value of the aberrations is 0.53 waves at λ_{HeNe} . The root mean square (RMS) value is 0.09 waves at λ_{HeNe} . The data shown correspond to maximum deviations of about 130 nm from the ideal parabolic shape [53]. This is of the same order of magnitude as reported for the parabolic mirror used in Ref. [54].

Based on these interferometry results we have produced a phase plate which nominally imprints the phase conjugate of the measured aberrations onto an otherwise flat phase front. The fused silica phase plate is produced in house by laser lithography and (selective) reactive ion etching. In order to check the quality of aberration compensation the phase plate is inserted into the interferometric setup between the parabolic mirror and the flat reference plate. While constantly repeating the interferometric measurement, position and orientation of the phase plate are optimized. As a first optimization criterion we take the reduction of the PV value of the aberrations while for the fine adjustment the RMS value is a better measure, since this is the quantity determining the Strehl ratio [57]. The final outcome of such a measurement series is depicted in Fig. 4b). The PV value of the aberrations is reduced to 0.45 waves at λ_{HeNe} . The RMS value shrinks to 0.033 waves at λ_{HeNe} . It should be noted that the seemingly small reduction of the PV value is due to effects occurring at the boundaries of the phase plate and the parabolic mirror. Neglecting the outer 0.5 mm of the aperture the PV value shrinks to 0.16 waves at λ_{HeNe} and the RMS value is reduced to 0.023 waves.

To judge the quality of these improvements we have performed simulations of the focal intensities based on a generalization of the method by Richards and Wolf [58]. We assume a wave front according to the aberrations shown in Fig. 4 to be incident on a perfectly reflecting parabolic mirror. The incident light wave is a radially polarized doughnut mode (see Eq. (7)) with the optimum beam radius. The resulting focal intensities are normalized to the focal intensity obtained for an aberration free wave front. This yields the Strehl ratios. At the testing wavelength of our interferometer (633 nm), the Strehl ratio is improved from 68% to 99% by using the correcting phase plate. In other words, the combined system ‘parabolic-mirror-plus-phase-plate’ is practically capable of diffraction limited focusing.

At the wavelengths for experiments with Ytterbium ions the Strehl ratios of the uncorrected mirror are 32% for 370 nm and 9% for 252 nm. Close to diffraction limited performance seems feasible in these cases if the phase plate is designed for the respective wavelength considering the corresponding refractive index of fused silica.

Besides that, a phase plate that perfectly compensates the aberrations at the testing wavelength λ_{HeNe} is also rather suitable at the wavelengths of the transitions T1 and T2. Assuming a phase plate working perfectly at the testing wavelength, we simulated the performance of the compound system ‘phase-plate-plus-paraboloid’ at

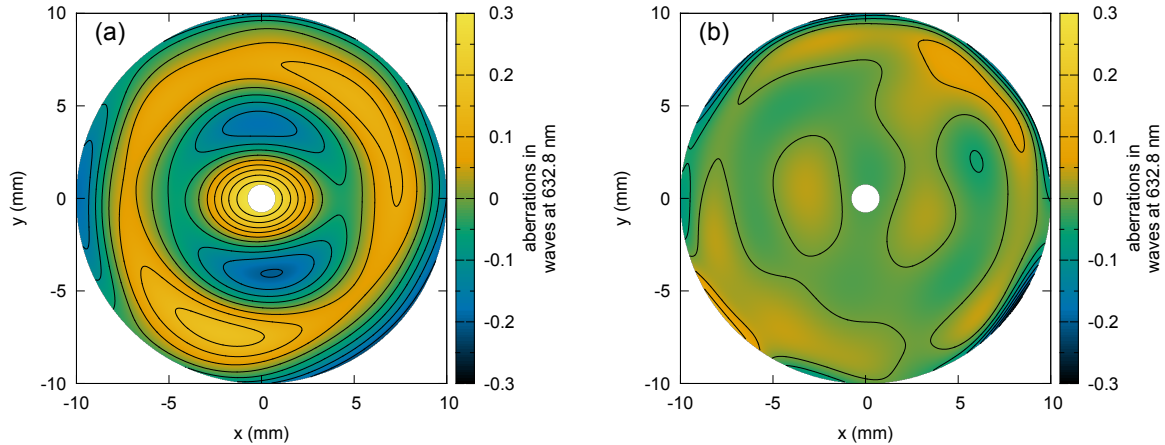


FIG. 4. (a) Measured phase aberrations in single pass reflection. The resulting aberrations are shown averaged over two different spheres and six rotational settings per sphere. The PV value is 0.53 waves. (b) Measured aberrations with a compensating phase plate (single experimental run). The PV value is 0.45 waves. In both panels the data result from a Zernike fit of degree 10. Adjacent contour lines are separated by 0.05 waves at λ_{HeNe} .

the other two wavelengths. Since the relative refractive index changes of fused silica at the wavelengths of interest are on the order of 1% – 3%, our simulations reveal Strehl ratios ranging from 97% to more than 99%, depending on the wavelength and the specific parabolic mirror.

So far we have assumed a phase shift upon reflection that does not depend on the distance to the mirror's optical axis. But due to the complex refractive index of aluminum this assumption is generally not justified. The radially varying phase shift upon reflection imposes a defocus. Nevertheless we argue that the influence of the refractive index of aluminum can be neglected. We calculate the phase shift upon reflection by taking the respective refractive indices from Ref. [59] and determining the argument of the complex reflection coefficient for electric fields parallel to the plane of incidence. For this we use the relations between angle of incidence and radial distance to the optical axis given in Ref. [23]. The obtained phase shifts are then used in simulations with an otherwise aberration free paraboloid. For the wavelengths considered here the simulations show an axial shift of the intensity maximum by less than a tenth of a wavelength. The maximum intensity is reduced by amounts on the order of 0.2% in the case of transition T2 and even less for the other wavelengths. The intensity in the nominal focus is reduced by 0.5% (1.5%, 2.8%) at the testing (transition T1, transition T2) wavelength.

The phase shifts induced by the above effects can in principle be measured by our interferometric setup. However, a substantial part of the treatment of the interferometric data is the removal of misalignment aberrations of the null sphere from the exact focal position [53]. Since the monotonous radial variation of the phase shift upon reflection is equivalent to a slight displacement of the null sphere, this effect is removed in the measurement procedure.

We finish this section by noting that the orders of mag-

nitude of the experimental results shown are generally reproduced for other parabolic mirrors, with the shape of the aberrations of the uncorrected mirrors differing from device to device.

V. GENERATION OF THE OPTIMUM TEMPORAL MODE

To design the temporal mode of a single photon wave packet that would be absorbed efficiently by a two level system, we exploit the time reversal symmetry of the compound system atom and free space field modes [24]. An excited two level atom spontaneously decays into the ground state under emission of a photon with a probability amplitude that is exponentially decreasing in time [60]. If a photon wave packet with such a decreasing envelope is sent onto a two level system the maximum possible excitation probability is calculated to be 54% [26].

An excitation probability of 100% is achieved by generating a photon wave packet with the time reversed shape of the spontaneously emitted photon: an exponentially increasing field amplitude with a time constant which is twice the lifetime of the excited state. Furthermore the ideal pulse length is infinite and has a sharp edge at the end. The excitation probability depends not only on a good overlap of the time constant and the sharp edge at the end of the pulse, but also on the total pulse length. In Ref. [26] it is shown theoretically that for pulse lengths of five lifetimes 99% excitation probability can be achieved. These numbers are valid for single photon Fock states. However, as outlined already in Sec. I, coherent state pulses with average photon numbers $\ll 1$ are a good approximation to single photon wave packets.

In the following, we discuss the generation of these coherent state wave packets. The experimental apparatus for the generation of arbitrarily shaped pulses is shown in

Fig. 1. A continuous wave laser beam is cut into pulses using an acousto-optic modulator (AOM). The intensity diffracted into the first order of the AOM depends on the amplitude U_0 of the applied radio frequency (RF) signal as $I(t) \sim \sin^2(U_0(t))$. An exponentially increasing wave packet is obtained by modulating the amplitude of the applied RF signal $U_{\text{RF}}(t) = U_0(t) \cdot \sin(\omega_{\text{RF}}t)$ as

$$U_0(t) = \arcsin \left(\exp \left[\frac{t}{2\tau} \right] \right) \quad (9)$$

where $\omega_{\text{RF}} = 2\pi \cdot 400$ MHz is the RF driving frequency of the AOM. The modulated RF signal is generated with a digital arbitrary waveform generator and amplified before being applied to the AOM. The first diffraction order of the AOM is coupled to a polarization maintaining single mode fiber and sent to the setup for the spatial beam shaping. The attenuation to a mean photon number per pulse of much less than one is done using a set of half-wave plates and linear polarizers. The temporal profile of these highly attenuated laser pulses is measured using a photomultiplier tube with a quantum efficiency of 15% and a frequency counter in start-stop configuration. Since we do not measure a photon in every pulse, the start trigger is given by the detection of a photon and the stop trigger by the following clock signal activating the output of the arbitrary waveform generator. We account for this trigger configuration by reversing the temporal coordinate of the experimental data. In Fig. 5 the measurements of the pulses designed to match the lifetimes of transition T1 and T2 are shown. The mean photon number per pulse is 0.09. For simplicity reasons the 370 nm laser was used for the creation of the pulses for both time constants.

The temporal overlap η_t of the field amplitudes is calculated according to Eq. (4). The incident field amplitude $E_{\text{inc}}(t)$ is obtained by taking the square root of the photon count statistics and the integration is performed over the time intervals covered by the experimental data shown in Fig. 5. The results of this procedure are $\eta_t = 0.96$ for the pulse with 8 ns time constant and $\eta_t = 0.99$ for the 230 ns pulse. The lower overlap value in the case of the 8 ns pulse is attributed to the finite build-up/decay time (5 ns) of the optical grating inside the AOM crystal. This results in non-negligible deviations from a sharp pulse end when compared to the time constant of the rising exponential.

VI. DISCUSSION

With the acquired experimental data at hand we are now able to give an estimate of the coupling efficiency and absorption probability which would be achieved in experiments employing the generated field modes. Table II summarizes the field overlaps of the generated light modes in time and in space domain, as well as the Strehl ratio. According to Eqs. (3) and (5) we calculate G

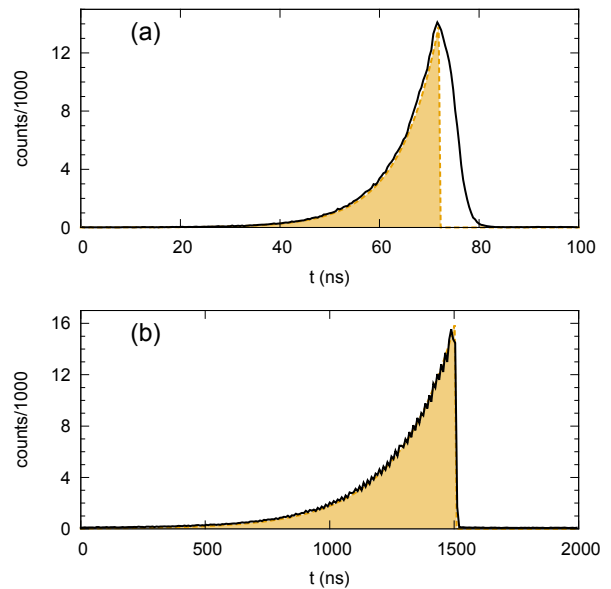


FIG. 5. Generated exponentially increasing pulses with a mean photon number per pulse of 0.09 photons. The dashed line indicates the perfect pulse shapes. The time constant (life time) is 8 ns in panel (a) and 230 ns in panel (b). The total number of counts are $430 \cdot 10^3$ and $487 \cdot 10^3$, respectively.

Transition	T1	T2
Spatial overlap η	0.979	0.975
Solid angle $\Omega_\mu / \frac{8\pi}{3}$	0.94	0.94
Strehl ratio	0.99	0.99
Temporal overlap η_t	0.96	0.99
Coupling strength G	0.892	0.885
Absorption probability P_a	0.812	0.867

TABLE II. Overview of the achieved figures of merit. The Strehl ratio is taken from the proof of principle experiment at λ_{HeNe} .

and P_a from these values and let the Strehl ratio enter as a multiplicative factor accounting for losses caused by the mirror imperfections remaining after compensation. We thus arrive at prospective coupling strengths of $G = 0.892$ ($G = 0.885$) for transition T1 (T2). These values are only about two percent below the upper limit set by the experimental geometry when using doughnut modes. The corresponding absorption probabilities are $P_a = 0.812$ ($P_a = 0.867$).

These absorption probabilities are valid under the assumption of a closed two-level system (e.g., transition T2 of $^{174}\text{Yb}^{2+}$). As an example for a more complex level structure we take the transition T1 of $^{174}\text{Yb}^{+}$: Both the excited and the ground state are split into two Zeeman sub-levels with the magnetic quantum numbers $m = \pm 1/2$ (we neglect the dipole allowed $^2P_{1/2} \rightarrow ^2D_{3/2}$ transition due to the small branching ratio of 0.5% [61]).

Two linear and two circular dipole transitions are possible. The probability for spontaneous decay via a linear dipole transition is $1/3$ according to the corresponding Clebsch-Gordan coefficient and $2/3$ via a circular dipole transition. Exciting the linear dipole transition leads to a maximum possible excitation probability of $1/3$, assuming the excitation light mode is ideal. In this sense, one has to understand the value $P_a = 0.812$ given for a mode designed for this transition as a relative value, i.e., the de facto absorption probability would be $P_a/3$. However, the coupling strength G itself is not affected by such considerations. For example, an elastic scattering experiment on any of these transitions should be feasible with the coupling strength derived for an ideal two-level system because no dipole moments are induced for transitions other than the driven one (cf. Ref. [62] for a calculation applying the level structure discussed above).

We conclude this paper by emphasizing that the method presented here to generate a dipole mode can be applied to a dipole transition at any optical wavelength.

An application to circular dipole transitions is straightforward requiring corresponding amplitude and polarization distributions. However, these polarization patterns become quite complex – especially when focusing from a large solid angle [43].

In summary, we have demonstrated the generation of modes of the electromagnetic field allowing for efficient coupling of single photons and single two-level systems in free space using a deep parabolic mirror. The free space coupling method described here should compete favorably with other coupling schemes.

ACKNOWLEDGMENTS

The authors acknowledge fruitful discussions with A. Villar, S. Heugel, M. Fischer and J. Schwider. M.S. acknowledges financial support from the Deutsche Forschungsgemeinschaft (DFG).

-
- [1] M. D. Lukin, *Rev. Mod. Phys.* **75**, 457 (2003)
 - [2] K. Hammerer, A. S. Sørensen, and E. S. Polzik, *Rev. Mod. Phys.* **82**, 1041 (2010)
 - [3] J. M. Raimond, M. Brune, and S. Haroche, *Rev. Mod. Phys.* **73**, 565 (2001)
 - [4] H. Walther, B. T. H. Varcoe, B.-G. Englert, and T. Becker, *Rep. Prog. Phys.* **69**, 1325 (2006)
 - [5] H. J. Kimble, *Physica Scripta* **T76**, 127 (1998)
 - [6] G. Rempe, *Contemporary Physics* **34**, 119 (1993)
 - [7] J. I. Cirac, P. Zoller, H. J. Kimble, and H. Mabuchi, *Phys. Rev. Lett.* **78**, 3221 (1997)
 - [8] H.-J. Briegel, W. Dür, J. I. Cirac, and P. Zoller, *Phys. Rev. Lett.* **81**, 5932 (1998)
 - [9] W. Dür, H.-J. Briegel, J. I. Cirac, and P. Zoller, *Phys. Rev. A* **59**, 169 (1999)
 - [10] C. W. Gardiner, *Phys. Rev. Lett.* **56**, 1917 (1986)
 - [11] G. Wrigge, I. Gerhardt, J. Hwang, G. Zumofen, and V. Sandoghdar, *Nature Physics* **4**, 60 (2008)
 - [12] A. N. Vamivakas, M. Atatüre, J. Dreiser, S. T. Yilmaz, A. Badolato, A. K. Swan, B. B. Goldberg, A. Imamoglu, and M. S. Ünlü, *Nano Letters* **7**, 2892 (2007)
 - [13] M. K. Tey, Z. Chen, S. A. Aljunid, B. Chng, F. Huber, G. Maslennikov, and C. Kurtsiefer, *Nature Physics* **4**, 924 (2008)
 - [14] L. Slodička, G. Hétet, S. Gerber, M. Hennrich, and R. Blatt, *Phys. Rev. Lett.* **105**, 153604 (2010)
 - [15] S. A. Aljunid, M. K. Tey, B. Chng, T. Liew, G. Maslennikov, V. Scarani, and C. Kurtsiefer, *Physical Review Letters* **103**, 153601 (2009)
 - [16] M. Pototschnig, Y. Chassagneux, J. Hwang, G. Zumofen, A. Renn, and V. Sandoghdar, *Phys. Rev. Lett.* **107**, 063001 (2011)
 - [17] P. Kochan and H. J. Carmichael, *Phys. Rev. A* **50**, 1700 (1994)
 - [18] S. J. van Enk and H. J. Kimble, *Phys. Rev. A* **63**, 023809 (2001)
 - [19] S. J. van Enk, *Phys. Rev. A* **69**, 043813 (2004)
 - [20] G. Zumofen, N. M. Mojarad, V. Sandoghdar, and M. Agio, *Phys. Rev. Lett.* **101**, 180404 (2008)
 - [21] M. K. Tey, G. Maslennikov, T. C. H. Liew, S. A. Aljunid, F. Huber, B. Chng, Z. Chen, V. Scarani, and C. Kurtsiefer, *New Journal of Physics* **11**, 043011 (2009)
 - [22] S. Quabis, R. Dorn, M. Eberler, O. Glöckl, and G. Leuchs, *Opt. Comm.* **179**, 1 (2000)
 - [23] N. Lindlein, R. Maiwald, H. Konermann, M. Sondermann, U. Peschel, and G. Leuchs, *Laser Physics* **17**, 927 (2007)
 - [24] M. Sondermann, R. Maiwald, H. Konermann, N. Lindlein, U. Peschel, and G. Leuchs, *Appl. Phys. B* **89**, 489 (2007)
 - [25] D. Pinotsi and A. Imamoglu, *Phys. Rev. Lett.* **100**, 093603 (2008)
 - [26] M. Stobinska, G. Alber, and G. Leuchs, *EPL* **86**, 14007 (2009)
 - [27] Y. Wang, J. Minář, L. Sheridan, and V. Scarani, *Phys. Rev. A* **83**, 063842 (2011)
 - [28] N. Piro, F. Rohde, C. Schuck, M. Almendros, J. Huwer, J. Ghosh, A. Haase, M. Hennrich, F. Dubin, and J. Eschner, *Nat. Phys.* **7**, 17 (2011)
 - [29] D. J. Wineland, W. M. Itano, and J. C. Bergquist, *Opt. Lett.* **12**, 389 (1987)
 - [30] M. Eisaman, A. André, F. Massou, M. Fleischhauer, A. Zibrov, and M. Lukin, *Nature* **438**, 837 (2005)
 - [31] J. F. Chen, S. Zhang, H. Yan, M. M. T. Loy, G. K. L. Wong, and S. Du, *Phys. Rev. Lett.* **104**, 183604 (2010)
 - [32] A. Kalachev, *Phys. Rev. A* **81**, 043809 (2010)
 - [33] A. Haase, N. Piro, J. Eschner, and M. W. Mitchell, *Opt. Lett.* **34**, 55 (2009)
 - [34] A. Kuhn, M. Hennrich, and G. Rempe, *Phys. Rev. Lett.* **89**, 067901 (2002)
 - [35] M. Keller, B. Lange, K. Hayasaka, W. Lange, and H. Walther, *Nature* **431**, 1075 (2004)
 - [36] J. McKeever, A. Boca, A. Boozer, R. Miller, J. Buck, A. Kuzmich, and H. J. Kimble, *Science* **303**, 1992 (2004)

- [37] J. Bochmann, M. Mücke, G. Langfahl-Klabes, C. Erbel, B. Weber, H. P. Specht, D. L. Moehring, and G. Rempe, *Phys. Rev. Lett.* **101**, 223601 (2008)
- [38] P. Kolchin, C. Belthangady, S. Du, G. Y. Yin, and S. E. Harris, *Phys. Rev. Lett.* **101**, 103601 (2008)
- [39] L. Orlslager, J. Cussey, A. T. Nguyen, P. Emplit, S. Massar, J.-M. Merolla, and K. P. Huy, *Phys. Rev. A* **82**, 013804 (2010)
- [40] N. Gisin, G. Ribordy, W. Tittel, and H. Zbinden, *Rev. Mod. Phys.* **74**, 145 (2002)
- [41] R. W. Berends, E. H. Pinnington, B. Guo, and Q. Ji, *J. Phys. B* **26**, L701 (1993)
- [42] Z. G. Zhang, Z. S. Li, S. Svanberg, P. Palmeri, P. Quinet, and E. Biemont, *Eur. Phys. J. D* **15**, 301 (2001)
- [43] M. Sondermann, N. Lindlein, and G. Leuchs, arXiv:0811.2098 [physics.optics] (2008)
- [44] Z. Bomzon, G. Biener, V. Kleiner, and E. Hasman, *Opt. Lett.* **27**, 285 (2002)
- [45] Z. Ghadyani, I. Vartiainen, I. Harder, W. Iff, A. Berger, N. Lindlein, and M. Kuittinen, *Appl. Opt.* **50**, 2451 (2011)
- [46] M. Stalder and M. Schadt, *Opt. Lett.* **21**, 1948 (1996)
- [47] R. Oron, S. Blit, N. Davidson, A. Friesem, Z. Bomzon, and E. Hasman, *Applied Physics Letters* **77**, 3322 (2000)
- [48] S. Tidwell, D. Ford, and W. Kimura, *Applied Optics* **29**, 2234 (1990)
- [49] S. Tidwell, G. Kim, and W. Kimura, *Applied Optics* **32**, 5222 (1993)
- [50] R. Dorn, S. Quabis, and G. Leuchs, *Phys. Rev. Lett.* **91**, 233901 (2003)
- [51] S. Quabis, R. Dorn, and G. Leuchs, *Appl. Phys. B* **81**, 597 (2005)
- [52] B. Schaefer, E. Collett, R. Smyth, D. Barrett, and B. Fraher, *American Journal of Physics* **75**, 163 (2007)
- [53] G. Leuchs, K. Mantel, A. Berger, H. Konermann, M. Sondermann, U. Peschel, N. Lindlein, and J. Schwider, *Applied Optics* **47**, 5570 (2008)
- [54] A. Drechsler, M. Lieb, C. Debus, A. Meixner, and G. Tarrach, *Opt. Express* **9**, 637 (2001)
- [55] J. Stadler, C. Stanciu, C. Stupperich, and A. J. Meixner, *Opt. Lett.* **33**, 681 (2008)
- [56] R. Maiwald, D. Leibfried, J. Britton, J. C. Bergquist, G. Leuchs, and D. J. Wineland, *Nature Physics* **5**, 551 (2009)
- [57] M. Born and E. Wolf, *Principles of optics*, 6th ed. (Pergamon Press, Oxford, 1991)
- [58] B. Richards and E. Wolf, *Proceedings of the Royal Society of London. Series A, Mathematical and Physical Sciences* **253**, 358 (1959)
- [59] D. Y. Smith, E. Shiles, and M. Inokuti, in *Handbook of Optical Constants of Solids*, Vol. 1, edited by E. D. Palik (Elsevier, 1998) pp. 369–406
- [60] V. Weisskopf and E. Wigner, *Z. Phys.* **63**, 54 (1930)
- [61] J. Migdalek, *J. Phys. B* **13**, L169 (1980)
- [62] L. Jin, Y. Niu, and S. Gong, *Phys. Rev. A* **83**, 023410 (2011)